Nucleation and 3D growth of *para*-sexiphenyl nanostructures from an oriented 2D liquid layer investigated by photoemission electron microscopy

2009 J. Phys.: Condens. Matter 21 445003

(http://iopscience.iop.org/0953-8984/21/44/445003)

J. Phys.: Condens. Matter **21** (2009) 445003 (11pp) doi:10.1088/0953-8984/21/44/445003

Nucleation and 3D growth of *para*-sexiphenyl nanostructures from an oriented 2D liquid layer investigated by photoemission electron microscopy

A J Fleming, F P Netzer and M G Ramsey

Surface and Interface Physics, Institute of Physics, Karl-Franzens Universität Graz, Universitätsplatz 5, 8010 Graz, Austria

E-mail: sandy_fleming@yahoo.com

Received 17 May 2009, in final form 28 August 2009
Published 9 October 2009
Online at stacks.iop.org/JPhysCM/21/445003

Abstract

The deposition in an ultrahigh vacuum of prototypical linear *para*-sexiphenyl (6P) molecules onto the anisotropic reconstructed surface of Cu(110)2 × 1–O presents an ideal system with reduced symmetry for investigation. A dynamic photoemission electron microscopy (PEEM) study of the nucleation and growth of 6P, combined with data obtained from static techniques, is shown to facilitate our understanding of the requirements for 6P nuclei formation and self-assembly into long anisotropic needles. High-rate image acquisitions in PEEM are shown to reveal dynamic phenomena, such as meta-stable layer de-wetting and nanostructure growth in real time, that are the result of nucleation and self-assembly processes. Furthermore, time dependent studies of the relaxation of the meta-stable layer give insights into the molecular diffusion kinetics, whereas temperature dependent studies allow nucleation energies and molecular binding energies to be quantitatively measured. The deposition of the first monolayer of material is found to assemble without the formation of islands until full coverage (1 ML) is achieved. The second layer fills homogeneously and remains in a liquid smectic phase until a total deposition of 1.95 ± 0.07 ML is reached, whereupon critical nuclei of 6P crystallize out of the 2D liquid layer. The maximum of the diffusion coefficient is estimated to be 2×10^{-9} cm^2 s^{-1}. The resulting de-wetting of the meta-stable second layer rapidly increases the size of the nuclei while maintaining the anisotropic needle nanostructure shape. Probing the de-wetting layer reveals that 6P diffusion is 1D up to 100 °C. The nucleation energy and intermolecular binding energy are measured to be 675 meV and 2.1 eV, respectively.

1. Introduction

A well understood and precisely controlled deposition of a small quantity of dielectric material onto a metal surface is a key step in the preparation of active and interfacial layers of organic electronic devices such as organic light-emitting diodes (OLED) [1] and organic field-effect-transistors (OFET) [2]. The semiconducting molecule *para*-sexiphenyl (6P) is an organic dielectric material [3] that has been extensively studied by various surface science techniques and has been shown to produce highly ordered films of 6P on certain substrates. Naturally this increases its attractiveness as an active blue light-emitting layer in optoelectronic devices for the purposes of polarized light emission [4]. Typically for OLEDs and OFETs, conductive inorganic substrates are employed as electrodes for charge injection and as templates for molecules to assemble on [5, 6]. Improving the performance of these organic devices requires adjusting general parameters such as the materials used and the resultant film morphologies. However self-assembly, a natural phenomenon at the nano-scale [7, 8], will inexorably couple these two particular parameters making it hard to control one without affecting the other. Understanding such a thermodynamically driven self-assembly process requires

that a large parameter space be explored. Nonetheless, if anisotropic molecules and anisotropic substrates are employed the system under study is simpler, and therefore greater insights into the self-assembly process are possible.

In this regard, photoemission electron microscopy (PEEM) is a surface sensitive technique that is ideally suited to monitoring the initial stages of growth of molecular films during deposition [9–12]. PEEM is sufficiently sensitive to image sub monolayer to several monolayers of deposited organic material [13], especially if careful selections of photon energy and metal substrate are made. When weakly bonded dielectric materials are deposited, as is the case with organic materials considered suitable for vacuum sublimation, the thermodynamic relaxation of the as deposited material may give rise to dynamic phenomena that can be monitored in real time using PEEM. These dynamic processes include spontaneous film de-wetting, nucleation and island/needle growth. It is an understanding of these initial stage phenomena that is crucial in determining whether true architectural control of organic films will be possible using only spontaneous self-assembly bottom–up approaches.

Anisotropic properties of surfaces and molecules are of particular interest in the development of low-dimensional molecular nanostructures. Needles are a common type of nanostructure that is routinely observed when anisotropic molecules are deposited on anisotropic surfaces. For instance 6P deposited on $TiO_2(110)$ [14], mica [15], Cu(110) and Cu(110)2 × 1–O [16] will self-assemble into nano-needles Furthermore, in terms of the self-assembly sequence, the choice of an anisotropic molecule/substrate combination permits the decoupling of the description of molecular interactions into two separate directions: (a) parallel [001] direction and (b) $[1\bar{1}0]$ perpendicular direction to the O induced surface corrugation. Although this decoupling will be shown to facilitate our understanding of the assembly process, the extended and linear shape of 6P molecules interacting with an anisotropic surface means that a standard hard-sphere atomistic approximation [17] is really not applicable. Likewise, classical nucleation theory, an effective tool in predicting growth behaviour, does not deal with the underlying kinetic mechanisms of growth [18]. Therefore, for our interpretation, we rely on trends observed from our data and some well founded assumptions of nucleation theory to propose and/or exclude possible growth mechanisms. This is aided by the fact that fully grown 6P nanostructures, identical to those investigated here, have previously been characterized in terms of their geometric and electronic structure, through various static techniques such as NEXAFS [5], STM [16], RDS [19] and ARUPS [20]. Given that the initial conditions and the final nanostructures are both well understood, the goal here is to make use of data from both static and dynamic techniques to establish what the growth mechanism of 6P nanostructures is—this includes the eventual aim of establishing some framework for future molecular dynamics simulations [21, 22].

In PEEM contrast results from lateral differences in photoelectron or secondary electron yields. Variations in yield arise from differences in workfunction or electron intensity attenuation on the surface. To obtain good PEEM images a high contrast is essential. This can be obtained either with energy filtering of photoelectrons or more efficiently by carefully selecting the illumination source photon energy. For *para*-sexiphenyl (6P) on a Cu(110)2 × 1–O substrate (figure 1(a)) the photon energy of an Hg discharge lamp is ideal for maximizing the contrast. The ionization potential of 6P molecules in lying monolayers and 6P $(20\bar{3})$ crystals is ∼6.12 eV [23] which is above the 4.9 eV photon energy whereas the workfunction of the substrate is below this energy and falls from 4.8 to 4.4 eV during deposition. The high contrast observed is the result of a relatively high photoelectron and secondary electron yield from the substrate, the absence of photoelectron emission from 6P and the effective attenuation by 6P of secondary electrons originating from the substrate. As can be seen in figure 1(b) this results in areas with a large surface density of molecules appearing dark. The advantage of this particular choice of molecule, substrate and photon energy is the richly detailed photoelectron intensity versus time curves that can be used to monitor the growth in real time and to determine the growth mechanism.

Obtaining a high contrast allows for shorter image acquisition times to be used (by sacrificing some contrast) and enables PEEM images to be taken on the timescale of dynamic processes governing 6P needle growth. Ultimately these processes lead to growth in the third dimension which is inaccessible with PEEM. However, the amalgamation of PEEM with surface scanning probe measurements performed by atomic force microscopy (AFM), extends the total characterization scale possible, from hundreds of micrometres down to nanometres, and enables the vertical dimensions of the nanostructures to be measured.

It will be shown that 6P molecules, upon deposition onto a clean Cu(110)2 × 1–O surface, initially assemble layer-by-layer up to two monolayers (ML) thickness. The second layer, inaccessible to static techniques, is observed by PEEM and will be shown to be in a 2D liquid state that is meta-stable. This will be argued to be due to substrate one-to-one-commensurate arrangements and bulk arrangements of molecules in the second layer being heavily stressed or otherwise energetically unfavourable. PEEM will be demonstrated to be capable of measuring the dynamic de-wetting that ensues once a critical second layer surface density is reached. At this critical point the strain is circumvented by the energetic stabilization of small 6P crystals and a spontaneous de-wetting by the second layer to form needles proceeds. The dynamic behaviour of the second layer molecules is also explored and found to demonstrate the existence of a preferable one-dimensional diffusion direction up to ∼100 °C. These needles continue to grow lengthwise much faster than in width or height (mainly due to sticking/binding anisotropy [24]) and eventually grow to several micrometres in length (figure 1(b)). The distribution of the needle nucleation sites will be shown to be temperature dependent whereby at higher temperatures fewer but longer needles grow, for the same deposited amount, than at room temperature. Furthermore, AFM images reveal that the needles are in fact comprised of many single crystallites of 6P with notable inter-grain boundaries. In addition, it will be shown

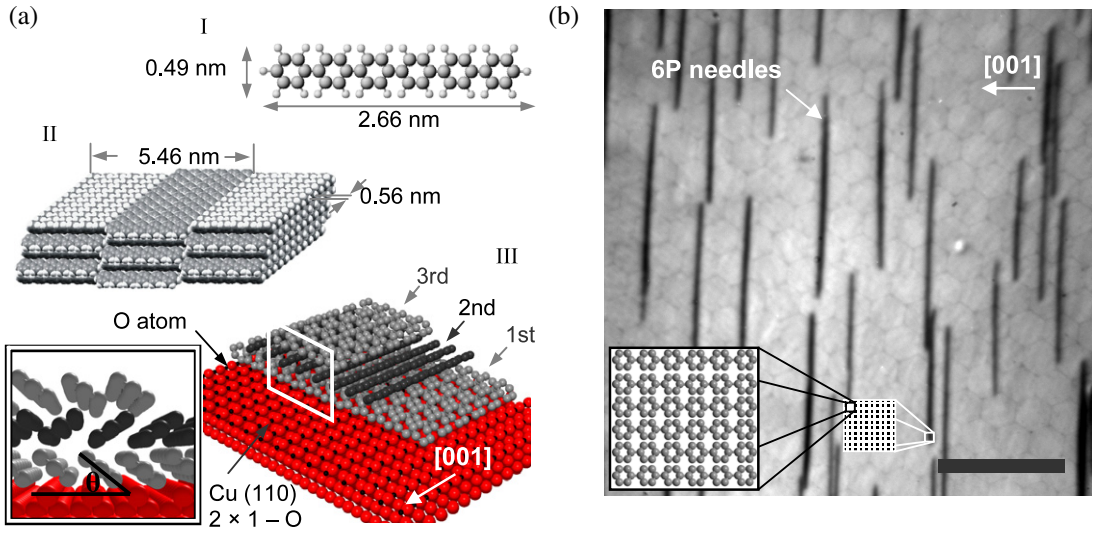

Figure 1. (a) (I) Molecular structure of *para*-sexiphenyl (6P) (dark grey—carbon, light grey—hydrogen). (II) Illustration of the bulk 6P crystal showing the orientation and $(20\bar{3})$ surface of 6P needles. Note the lying down and tilted orientation of 6P molecules. (III) The Cu(110)2 × 1–O reconstructed surface with two layers of the bulk 6P $(20\bar{3})$ crystal on top of the first layer on the surface. Note that for clarity purposes hydrogen atoms are excluded and alternate molecular layers are coloured dark/light grey. Inset: side-view illustrating the alignment of first 6P layer with the surface corrugation with two layers of the bulk crystal assembled on top. The molecular short axis tilt angle, θ, is shown. (b) Still image from PEEM growth video, after deposition of 6 ML, demonstrating the well ordered $(20\bar{3})$ oriented crystalline needles that form when 6P self-assembles on Cu(110)2 × 1–O at 140 °C (scale bar 10 μm). Note that the needles are dark and the wetting monolayer between the needles is bright. The [001] Cu crystallographic direction of the O induced surface corrugated reconstruction is indicated. The faint hexagonal pattern in the image is the outline of the micro-channel plate image intensifier and is unrelated to the surface. Inset: top-view of the top layer of 6P $(20\bar{3})$ crystal in (a)—III arranged to show the orientation of molecules that form the needles.

(This figure is in colour only in the electronic version)

that the dynamics of needle break-up, upon desorption of 6P molecules near the sublimation temperature, allows the molecular binding energy to be determined.

2. Experimental details

The experiments were performed in a custom-designed, combined Omicron VT-AFM/scanning tunnelling microscopy (STM)-PEEM UHV instrument [25] with a base pressure $< 2 \times 10^{-10}$ mbar. The Cu(110) crystal was cleaned in five steps, namely (a) flashing of the crystal to above the desorption temperature of 6P (>220 °C) to reduce the amount of 6P on the crystal before sputtering, (b) mild Ar^+ sputtering (10 μA, 1.5 kV, 45 min) followed by (c) annealing for 5 min at 500 °C (d) cooling in oxygen atmosphere at 5×10^{-7} mbar for 5 min and (e) flashing to 500 °C. Several cycles of the cleaning steps (b) through to (e) were performed with the final cleaning cycle omitting (d) and (e). These cleaning steps result in a clean Cu(110) surface. The 2 × 1–O reconstruction was prepared by dosing ∼15 l O_2 soon after step (c). Following cleaning, the sample was transferred, via a magnetically coupled transfer rod, to the PEEM.

The molecular evaporator, mounted *in situ* and facing the sample holder of the PEEM, consists of a Knudsen type effusion cell resistively heated by current supplied to a filament by a constant-current source. The 6P in powder form, supplied by TCI chemicals (Japan) and introduced previously into the Knudsen cell, is degassed thoroughly by extended heating just below the sublimation temperature of 6P. The first few 6P films deposited are not used for measurements. There is no quartz thickness monitor available due to space restrictions so no instantaneous deposition rate monitoring is possible. However, the constant-current supply allows the heating of the evaporator to be stabilized to a given temperature, which when combined with the accurate photoemission intensity versus time curves (see section 3) allows for an accurate *a posteriori* calculation of the stabilized deposition rate. A mechanical shutter, open throughout the entire deposition, allows the deposition time to be accurately controlled. The shutter is also used to open and close periodically to probe molecular diffusion.

PEEM measurements were carried out using a FOCUS/Omicron PEEM instrument in high magnification mode using a Mercury HBO 103W/2 discharge lamp (maximum of 4.9 eV) for illumination at angle of incidence of 25°. For the molecule/substrate combination used here the image contrast in PEEM makes use of laterally distributed local work-function differences that result in varying yields of photoelectrons. Since an optical illumination source is used, reflectivity differences of the surface also contribute to the final image in the form of topological contrast. An aperture size of 50 μm together with a fully open iris gave the optimal resolution for images with a pre-calibrated (in-house) field-of-view of 20–70 μm. Extractor voltages of 10.5–13.5 kV were employed, with a sample–extractor distance of 1.8 mm. No adverse effects, such as decomposition or desorption, arising from the UV light or high electric field were observed for 6P on Cu(110)2 × 1–O. Photoelectron intensities plotted in section 3 were acquired directly from intensity averaged areas of

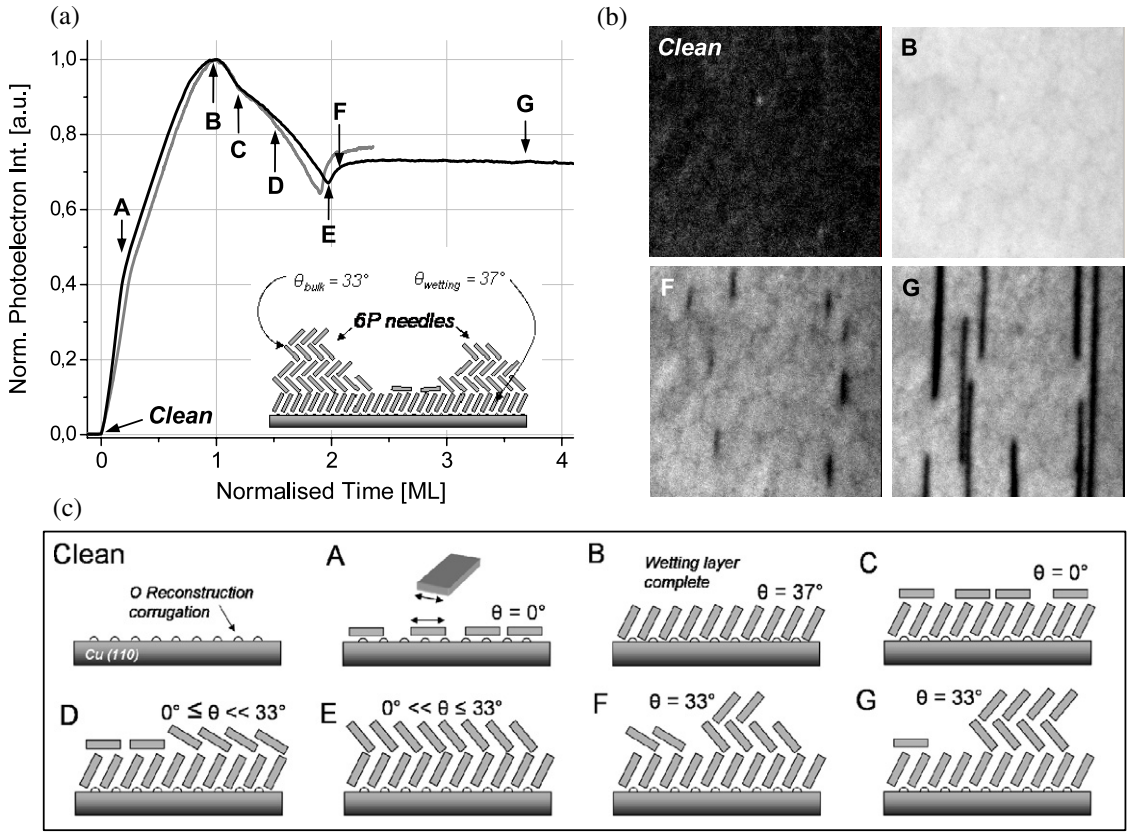

Figure 2. (a) Two typical plots of the photoelectron intensity versus normalized time in ML corresponding to two separate depositions of 6P at 140 °C. Unless otherwise stated, all discussions in the text refer to the black curve. The change in workfunction from clean substrate (4.8 eV) to timeline point B is ~ -0.4 eV. 1 ML converted to time is ∼180 s. No differences were observed in the trends of the intensity versus time curves that could be attributed to a different deposition rate. Inset: schematic illustrating the structure of the various layers that assemble. Note: the evaporator shutter is continuously open. (b) Snap-shot 15 μm $\times$ 15 μm images from PEEM video of the surface at each key stage of the deposition timeline. (c) Schematic diagrams illustrating (molecular end-on view only) the various orientations and packing changes that explain the shape of the photoelectron intensity versus normalized time plot. The short axis of the 6P molecule is illustrated by a double-headed arrow. The packing angle θ is the angle between the molecular short axis and the surface. The O induced corrugated surface reconstruction is indicated by showing the end atoms of extended O rows (which run into and out of the printed page). The distance between adjacent rows is 5.1 Å.

the PEEM images. Area averaging of the intensity works well up to the point where dark structures form on the surface. Once dark structures start growing, area averaging of the intensity to determine the surface molecular density will become distorted by the coverage of the dark structures. At 140 °C the ratio of dark structures to bright area is small; therefore the error introduced is also small. A video camera exposure time of 500 ms at an acquisition rate of 2 Hz was found to be adequate to monitor dynamic processes on the surface. *In situ* sample heating was achieved by indirect heating with a filament following a pre-determined and calibrated temperature–time curve.

AFM images, of the samples grown *in situ* in the PEEM instrument, are acquired in amplitude regulation mode with a frequency shift ranging from 50 to 500 Hz. This unusual UHV AFM scanning mode is found to perform best for the relatively tall (50–100 nm) 6P nanostructures that form on the surface. The usual FM regulation control software/electronics, mostly suited to imaging very flat structures, is incapable of stably imaging 6P needles in UHV. Therefore, an in-house modification, whereby the damping signal is fed into the usual FM modulation electronics/software is employed. Further careful electronic optimization of gain, phase and laser spot intensity results in cantilevers achieving oscillation and successfully approaching the surface. As a result of the high Q factor oscillation of cantilevers in UHV, the large dynamic range of frequency shift produces extremely sharp images with an added stable regulation provided by the fact that, in UHV, the cantilever amplitude does not change quickly. Due to the insulator properties of the dielectric material and the charge build up associated with scanning in UHV, a bias voltage of 0.1–3 V is also required for stable scanning.

3. Results and discussion

3.1. Photoemission intensity evolution

Typical plots of the area averaged photoelectron intensity versus time when 6P is deposited at 140 °C are given in figure 2(a). Three distinct stages are observed, namely (1) a sharp rise in intensity, (2) a maximum with a subsequent decrease in intensity, and (3) upon reaching a critical deposited amount, a sharp dip and small increase in intensity followed

by a constant gentle rise in intensity thereafter. These are the typical features observed when 6P is deposited on Cu(110)2 × 1–O in the temperature range from 25 to 150 °C. Although two curves are shown in figure 2(a), to illustrate the reproducibility between depositions, only the black curve will be discussed from hereon in the text (unless specifically mentioned otherwise). The timeline of events of the deposition begins with opening the molecular beam shutter. This initiates a sharp rise in intensity that results from lowering the workfunction further below the photon energy from 4.8 eV (clean substrate) to 4.4 eV (complete 6P monolayer). When 6P is deposited on a metal surface the surface dipole component of the metal workfunction decreases and in the process leads to an increase in secondary photoelectron yield which is observed as an intensity increase up until the moment the monolayer is completed.

Throughout the deposition timeline, the constant deposition rate linearly increases the number of molecules on the surface. It is the amount of dielectric per unit area on the surface, from hereon referred to simply as the density, which will determine the photoelectron intensity per unit area. Several static techniques such as NEXAFS [5], ARUPS [20] and STM [16], have established that 6P from monolayers to thick films is in a lying down and tilted orientation on Cu(110)2 × 1–O. In this orientation the long axis is parallel to the substrate and the density of a fully packed 6P layer is determined by the tilt angle, θ, of the short axis molecular aromatic plane with respect to the surface (see figure 1(a)). A fully packed layer comprised of flat-lying $\theta = 0°$ molecules will therefore have a density that is less than the density when $\theta > 0°$ (the same applies for a 2D liquid where θ is an average tilt angle). For large angles, the spacing between molecules S is given by $S = T(\sin\theta)^{-1}$ for $S < W$, where T is the molecular thickness (T is taken to be the intermolecular distance in figure 1(a) III) and W is the width of the 6P molecule along it's short axis.

Looking at figure 2(a), there is a kink in the plot at 0.2 ML which occurs at timeline point A. This kink indicates that a sudden change in the rate of increase of density takes place after 0.2 ML of material is deposited. This is explained by a sudden molecular rearrangement of the dilute layer that results in a change of average θ. As the deposition continues, more molecules arrive driving up the intensity up to point B where the maximum intensity is reached. As will be confirmed, the maximum at point B not only indicates that the first layer is complete (1.0 ML) but more importantly that the maximum density of the first layer has been reached. A key result to be remembered from this stage of the deposition is that no inhomogeneities or nanostructures are observed on the surface up to point B (see figure 2(b)).

Interestingly, a similar kink in the slope of the intensity versus time is observed further on from point B in the deposition timeline at around 1.2 ML (figure 2(a) timeline point C). This corresponds to 0.2 ML of material deposited on top of the first completed layer (1.0 ML). Both kinks observed (timeline points A and C) occur at +0.2 ML and both lead to a slowing down of the rate of intensity change with time. Hence the kink at C can be attributed to a similar packing rearrangement as that responsible for A in the timeline. A plausible reason for a sudden change in θ is that molecules in a dilute layer (where pairing is not yet favourable) will diffuse in a flat orientation, at least until enough molecules are present to start pairing and/or packing loosely with $\theta > 0°$. Thus the presence of a feature indicating a change in θ seems to correlate well with the dilute density of molecules that is expected for a layer that is just beginning to fill. Furthermore, the transformation of the trend from intensity increasing (surface dipole modification) to intensity decreasing (attenuation) at point B, confirms that the completion of the first layer is achieved at point B. This is the basis for the time normalization of the plot in figure 2(a).

From point B to E in the deposition timeline, an attenuation of secondary photoelectrons by second layer molecules leads to an overall decrease in the photoelectron intensity. A mechanism for this attenuation is the inelastic scattering of secondary photoelectrons involving energetic losses to inter-band transitions in 6P [26] (electronic band-gap ∼3.9 eV). If a significant portion of the 6P scattered secondary electrons have energies below the workfunction (4.4 eV) then the photoelectron yield and hence the intensity will decrease.

The feature at point E, which shows a rapid reversal of the trend from decreasing to increasing photoelectron intensity, is a sure indicator that the density of molecules in the second layer is now beginning to decrease. The appearance of nanostructures (image F in figures 2(b) and 3) indicates that a critical point, namely E, is reached whereupon the spontaneous nucleation of 6P into stable nanostructures becomes favourable. The formation of nanostructured needle nuclei on the surface leads to a spontaneous de-wetting of the second layer to form large microscopic needles on the surface (figure 2(b) E–F–G and figure 3). There is some small variability between depositions in the position of timeline point E. For instance de-wetting begins at 1.90 ± 0.01 ML and 1.97 ± 0.01 ML for the grey and black curves, respectively, in figure 2(a). The observed average position in time of timeline point E, from several depositions, is 1.95 ± 0.07 ML. This indicates that for 6P on Cu(110)2 × 1–O, on average, the critical density of the second layer required for spontaneous de-wetting (0.95 ML) is 5% less than the density of the first layer beneath (1.0 ML). From XRD and STM, the $(20\bar{3})$ surface of the bulk crystal of 6P has been measured to have a surface density of 0.647 mol nm^{-2}, which is 10% lower than the first layer density [16]. Thus it is reasonable to conclude that the requirement for needle formation is the prearrangement of molecules into roughly the required bulk structure. Below this critical density needles do not form. Nevertheless, once the needles are formed they continue to grow even when the density falls below the critical density. The reasons for this are discussed next.

3.2. Nucleation of para-sexiphenyl

In the following discussion the term nucleation refers to the aggregation of molecules where the aggregate lifetime is greater than the inverse of the collision rate of molecules diffusing on the surface. Below a critical density, spontaneous nucleation and de-nucleation occurs at a rate determined by

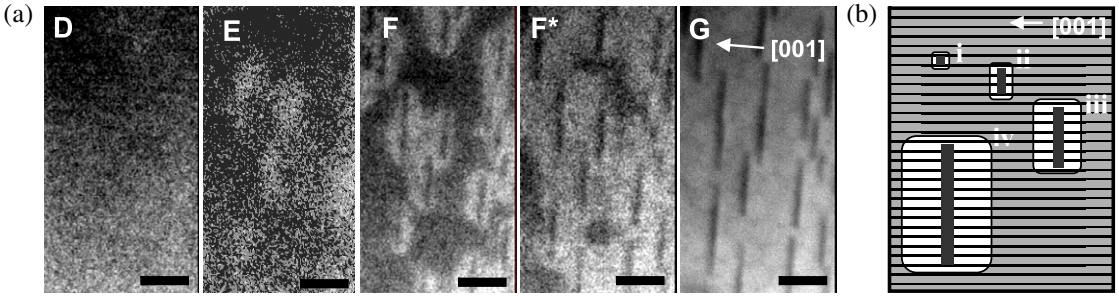

Figure 3. (a) PEEM images showing snapshots taken during the spontaneous de-wetting of the meta-stable second layer. The total time for de-wetting is ∼15 s. The naming scheme used is identical to that of figure 2 to allow comparisons. Image F* represents a point in the timeline a few seconds after F in figure 2. Images E and G have been, respectively, sharpened and time averaged. The scale bar is 5 μm. (b) Schematic diagrams illustrating the anisotropy of the de-wetting interface surrounding the needle with respect to the surface corrugation of the first molecular layer (as indicated by horizontal black lines). The progression in time is indicated by the sequence i–iv. The de-wetting interface is much closer to the top and bottom edges of the needle compared to the side edges. This indicates that the velocity of the de-wetting interface is greater in the direction parallel to the O rows than the perpendicular direction. The shaded area represents the de-wetting second layer, whereas the bright area is the exposed first monolayer.

the collision rate (including the sticking coefficient) and the de-binding rate, respectively. Both collision and de-binding rates are temperature dependent, but the collision rate is also a function of the layer density. The collision rate is proportional to $\rho\eta\sigma D_0 \exp(-E_D/kT)$ and the de-binding rate is proportional to $2\pi r \nu_0 \exp(-E_B/kT)$, where ρ is the surface molecule density, η is the sticking coefficient, σ is a geometry dependent collision cross-section, D_0 is the diffusion attempt frequency pre-factor, E_D is the energy barrier for diffusion, r is the nucleus radius, ν_0 is the frequency attempt pre-factor, E_B is the intermolecular binding energy, k is Boltzmann's constant and T is temperature in degrees kelvin. For this reason, at densities below the critical density, the rate of nucleation is lower than the rate of de-nucleation and no structures that form spontaneously *survive a long enough time* to grow and reach the critical nucleation size needed for an energetically stable structure to form on the surface.

For structurally commensurate homoepitaxy deposition the minimum critical nucleation size is two—no matter where a molecule binds on the crystal, the crystal + molecule structure formed will be energetically stable. Conversely, to form a long lifetime aggregate with an equilibrium number of two molecules that is structurally not energetically stable (i.e. where the cohesion energy is too low for a given growth temperature) a faster collision rate will be required in order to compensate for the faster de-binding rate. If a high surface density enables a critical nucleus size to be reached, the nuclei will be energetically stable and continue growing at the given growth conditions—even if the surface molecular density lowers. Hence, a high surface density that provides a high enough collision rate will *temporarily* kinetically stabilize energetically unstable nuclei until a critical size is reached. The probability of this occurring is vastly improved if (a) the molecules are pre-aligned (for instance on an anisotropic surface) and (b) the molecules are very close together to begin with. For 6P on Cu(110)2 × 1–O both these conditions are met at point E in figure 2.

The critical nucleus stability may be conferred in several ways: (a) by the packing structure increasing the binding energy of the molecules or (b) by the fact that proportionately fewer molecules reside on the surface (or perimeter) of large nuclei compared to the bulk of nuclei (and thus fewer are available to de-bind). Therefore it follows that once nuclei have grown larger than a critical size, nuclei do not require any further kinetic stabilization—as demonstrated by the continuous growth of the needles after the second layer density is reduced by the de-wetting process. Therefore at point G in figure 2 the growth regime is homoepitaxial growth with bulk 6P structure since all molecules arriving on the surface will diffuse until they bind to the 6P needle $(20\bar{3})$ surface.

Bearing in mind the above argument, the high second layer density required for 6P to initiate nucleation can be explained in terms of the possible structures that could form on the surface. Molecules in a dilute second layer that collide and temporarily bind can either attempt to arrange one-to-one commensurately to the first layer or in a bulk arrangement (which is not one-to-one commensurate or possibly incommensurate). However, for the second layer there is no stabilizing molecule to Cu(110)2 × 1–O surface interactions. Thus the difference in cohesion energy between a commensurate first layer and potentially commensurate second layer would, in the absence of a stabilizing substrate interaction, manifest itself as stress in the second layer. It is this uphill energy cost of forming a stressed full coverage second layer that prevents the spontaneous crystallization of a commensurate arrangement. The fact that, above the wetting monolayer, subsequent whole layers do not crystallize and continue growth as layer-by-layer demonstrates the countering effect of the strain energy. Likewise, a spontaneous bulk arrangement is also suppressed for *sub-critical* nuclei sizes that form during random molecular collisions in the dilute second layer. This is due to the unfavourable interaction that would arise from incommensurate (or less than one-to-one commensurate) arrangements with the first layer. In fact, if there were no uphill energy costs to crystallization for a dilute layer, then an inhomogeneous coverage of the second layer with islands growing over time would be observed (especially if the nucleation density were as low as for needle growth at

high temperature). This is not observed within the resolution of PEEM. The second layer is thus retained in a commensurate 2D liquid phase until a critical density is reached and hence the second layer is termed *meta*-stable.

In terms of the first layer, the 6P interaction with the Cu(110)2 × 1–O surface must hinder the formation of a bulk arrangement—even when the bulk density is exceeded—since the commensurate arrangement is only stabilized when the angle θ reaches 37°. This is why no de-wetting phenomena and no inhomogeneities are observed between 0 and 1 ML in figure 2 during deposition of the first layer. Nevertheless, once the first layer is fully packed it remains a stable wetting layer, even at temperatures above the bulk 6P desorption temperature (∼220 °C), as confirmed by static techniques such as STM, UPS and NEXAFS. However static techniques have not yet observed the second layer or the second layer de-wetting phenomenon that is clearly seen as a growing area of brightness surrounding the needles in figure 3. As shown in figure 3(a) D, the second layer density also increases homogeneously over the surface with time until the density of the bulk 6P arrangement is approximately reached. However, it is at this timeline point E that the 2D liquid crystallizes into energetically stable nuclei, with a bulk 6P arrangement, to form small needles which lead to the spontaneous de-wetting as mentioned previously (see figure 2).

3.2.1. Are the critical nuclei 3D or 2D? Since the 3D growth of bulk 6P needles is the direct result of the 2D second layer de-wetting, the following question arises: does the critical nucleus have a 2D or 3D structure? PEEM images in figure 3(a) clearly show that until some de-wetting occurs there is no possibility of observing an outline of any kind of nucleus (lateral contrast from differences in secondary electron yield is required). For example in figure 3(a) F, judging from the relative area of the de-wetted second layer zone compared to the area of the needle, the height of the needle is roughly 2–3 ML. Therefore a direct observation of the 2D or 3D critical nucleus before de-wetting is not possible. However PEEM data does afford more clues—which we will explore with the aim of establishing some framework to begin suitable molecular dynamics simulations of 6P self-assembly.

It is useful to consider what happens when a molecule arrives from the evaporator and lands on top of a 2D *liquid* layer. From figures 2 and 3, even with the molecular shutter continuously open, clearly no nucleation begins until timeline point E. The gradual increase in layer density, for the first and second layer without any visible nuclei forming, indicates that the minimization of the surface free energy makes molecules incorporate themselves into the layer without any crystallization occurring. This also applies to molecules that climb up into the third layer and then re-incorporate back into the second layer. The ability of molecules to climb up to a higher layer is clearly illustrated in figure 3(a) by the de-wetting of the second layer. The fast speed of de-wetting also demonstrates that molecules can move quickly into the third or higher layers. It is reasonable to expect that molecules in the third layer will behave similarly to molecules in the second layer. From the data, this implies that in a dilute third layer molecules diffuse, on average, in a flat orientation and that higher layer densities are required for temporary pairing of molecules or other rearrangements where molecules have $\theta > 0°$. Hence, as with any given layer, a certain critical density of molecules is required for molecules to crystallize in the layer.

With this information the case for a 3D critical nucleus can be examined. The crystallization of a 3D critical nucleus requires the participation of at least one third layer molecule. Semantically this implies two things: (a) whatever the molecule climbs on top of to populate the third layer is not yet a stable structure and (b) only when a third layer molecule arranges itself into a 3D bulk structure with the underlying second layer molecules does a 3D critical nucleus form. In light of the experimental data, there are several problems with this. If the second layer is still in a 2D liquid state when the molecule climbs on top then why would the molecule not incorporate itself back into the second layer? Perhaps if the second layer density is near its maximum density then the molecule that climbs on top may stay in the third layer, but it will need several other third layer molecules to be present close by (i.e. a high enough layer density) for a rearrangement to take place whereby the third layer tilt angle reaches the bulk angle of 33° (such as the rearrangement illustrated in figure 2(c) C, D and E). How can this high third layer density be reached, if the probability of climbing on top and staying on top, in the absence of a stable 2D platform underneath, is expected to be low? Since there is no evidence of a molecule from the evaporator landing on the second layer and initiating nucleation (no structure up to point E in figure 2) and it is unlikely that the number of molecules in the third layer can reach the required density to initiate a large change in θ, it appears that a 3D *critical* nucleus is unlikely. On reflection, the scenario that seems most plausible is the following.

3.2.2. Nucleation mechanisms. Below the critical density the molecules are in a 2D liquid state with randomly staggered intermolecular overlaps such as in a smectic phase, and hence have little or no long-range order along the [001] direction (they only have orientation order due to the anisotropy of the molecule and substrate). As more molecules are deposited the second layer becomes denser by packing molecules closer together with a smaller spacing S while increasing the average tilt angle θ. The sliding displacement along the short axis of the molecule as θ increases in turn leads to a greater intermolecular π-orbital overlap which leads to a stronger intermolecular binding (figures 1(a) and 2(c) D and E). Nevertheless, the actual intermolecular binding between molecules is also determined by the lateral overlap along the long axis of the molecule. The total intermolecular overlap area α is given by $\alpha = L(W - (T \tan\theta))$, if $\sin\theta > T/W$, where L is the length, W is the short axis width and T is the thickness, of the molecule. Statistically, certain regions in the layer will have molecules in preferred arrangements with a greater overall overlap. For 6P on Cu(110)2 × 1–O, regions with the strongest molecular binding are eclipsed with $\theta = 33°$. This is the required alignment for a 2D sheet of the $(20\bar{3})$ crystal. As discussed earlier a larger θ and

hence α does not necessarily guarantee stability since the interaction with the first layer surface corrugation will also play a role.

For any given tilt angle any regions where molecules have an optimal long axis overlap will survive longer as a nucleus (the binding energy is high hence the rate of de-binding is low). Therefore, as the tilt angle of bound molecules increases, so does their lifetime as bound entities increase. This lifetime is crucial for the next step that involves all the molecules that surround the nucleus that are still in a 2D liquid state. The molecules loosely bound to other molecules in regions surrounding the longer lifetime nucleus have smaller intermolecular π-orbital overlaps and will therefore be weaker bound, have much shorter lifetimes as bound entities and as a consequence will be very mobile (as demonstrated by the fast de-wetting of the second layer once critical nuclei form).

An important outcome of molecules crystallizing into strongly bound 2D nuclei is that bound molecules are less able to move independently from each other and hence they are immobile. This means that the surrounding molecules experience less collisions from molecules bound in the nucleus. Therefore, as soon as the more strongly bound long lifetime (and hence meta-stable) 2D nucleus forms, suddenly all the surrounding molecules experience a net diffusion driving force pushing them towards the nucleus along the corrugation grooves in the [001] direction. A much smaller contribution will arise from the perpendicular direction [110] due to the fact that if molecules move into the third layer from this direction the space left behind it will be partially filled by molecules from the 2D nucleus by reducing θ. The effect will be to severely reduce the lifetime of the 2D nucleus.

The net force on molecules results from the thermal motion of unbound molecules giving rise to a biased random walk towards the nucleus, hence the net driving force will be larger for high surface densities and high temperatures. If this driving force is sufficient, given the mobility of 6P molecules, to move enough molecules on top of the 2D critical nucleus during the lifetime of the 2D critical nucleus, then a stable 3D nucleus will form. It is this driving force that explains how a large enough number of molecules can move into the third layer, in a fast de-wetting process, to create a high enough third layer density for molecules to arrange into the bulk structure (with $\theta = 33°$). It is therefore evident that in the two step process of forming bulk type 3D needles, the first required step is the formation of a 2D critical nucleus to act as a stable platform. The net driving force that pushes molecules to climb on top of the 2D critical nucleus and form a stable 3D nucleus is a diffusion process that results from the non-equilibrium surface density gradient at the interface of the nucleus and the surrounding 2D liquid as soon as crystallization begins. As the de-wetting proceeds the net driving force will keep decreasing in tandem with the 2D liquid layer density decrease. The shape of the 3D nucleus will also play a role since the more layers a molecule must climb above to crystallize the slower the process will be (the mobility of the molecules on the steps and terraces up to the upper most layer may be much slower).

3.3. Second molecular layer spontaneous de-wetting

As shown in figure 3 the bulk needles 'seeds' that form grow rapidly in dimension as more molecules arrive from the second layer and stick (see figure 2(b)). Since a co-facial packing maximizes the binding energy, it is this binding anisotropy of the molecules which leads to the formation of anisotropic needle like structures [24]. The growth rate of the needles is very large at the start of the de-wetting process since a high density of molecules is needed on the surface to reach the critical density (see the uniformly dark image D in figure 3). The large scale mass transport that ensues is diffusion driven by the lateral concentration gradient perpendicular to the de-wetting interface as illustrated in figure 3 (the boundary of the bright/dark areas). This de-wetting interface begins at the nucleation centre and moves outwards more rapidly in the direction parallel to the O rows when compared to the perpendicular direction [27] (see figure 3(b)). This molecular diffusion anisotropy on the surface of the first wetting layer confirms that 6P molecules align with the O rows. Molecules diffusing in a 1D random walk will travel a distance given by $(2Dt)^{1/2}$, where D is the diffusion coefficient and t is time. For de-wetting molecules located mid-way between two adjacent needles (along the [001] direction) the minimum travel distance to reach a needle is equal to half the inter-needle distance. In figure 3(a), the average distance between needles is $\sim$5 μm for this particular deposition. Given that the de-wetting time is roughly 11 s long (between the needles), this translates into $D_{\max} \sim 2 \times 10^{-9}$ cm^2 s^{-1} at 140 °C. This is upper limit is half an order-of-magnitude less than D measured [28] for the small molecule CO on Pt (110) at $\sim$140 °C. An estimate of the total molecular flux from the second layer to needles during de-wetting is 6×10^{12} mol cm^{-2} s^{-1} which is factor $\sim$20 larger than the flux from the evaporator to the substrate which is $\sim 3 \times 10^{11}$ mol cm^{-2} s^{-1} (where mol is molecules).

When de-wetting, the density of the second layer decreases very rapidly (figures 2 and 3 E–F) as molecules continue binding to the needle until the rate of molecules binding equals the rate of molecules de-binding (figure 2 timeline point G). Hence the rapid rise in the photoelectron intensity in figure 2 upon de-wetting (timeline point E) that is observed to slow down over time as equilibrium is reached (even though the molecular evaporator is continuously open). Note that the rate of molecules de-binding is determined by the surface area of the needles (there are many molecules trapped under the surface of the needle that make up the bulk of the needle). The equilibrium density of molecules in the second layer can only be reached when these rates are in balance and include the arrival rate of molecules from the molecular evaporator. This equilibrium density can therefore be probed by opening and closing the molecular beam shutter as will be described next. Once the density of molecules on the surface and located in the space between the needles has equilibrated then all subsequent molecules deposited contribute only to the needle growth. No new nucleation sites develop once the initial nucleation has taken place since it is impossible to build up the required critical density, at the same growth temperature, in the presence of needles acting as sumps. Therefore, at point G in figures 2 and 3, the rate of growth of the needles is

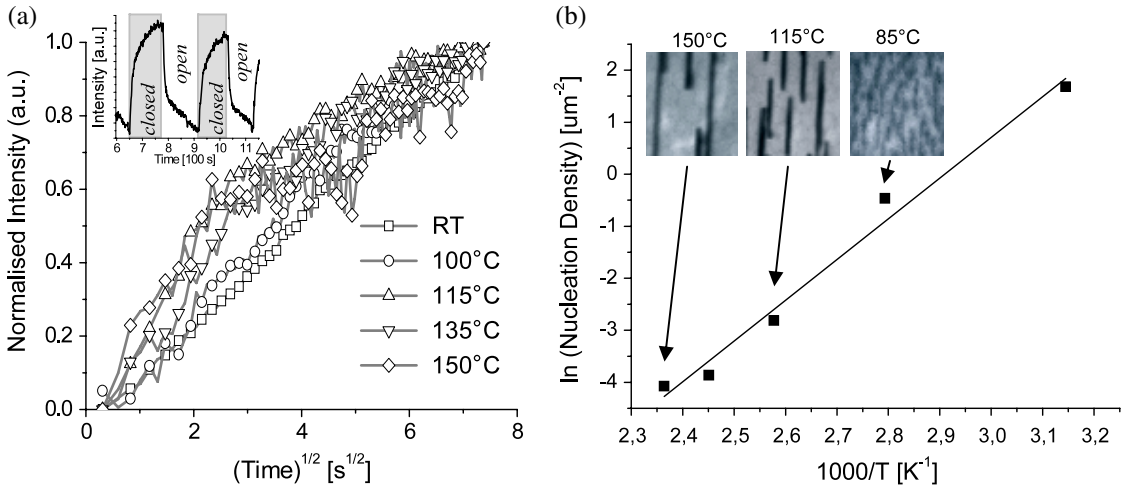

Figure 4. (a) Photoelectron intensity versus square-root-time at various temperatures, taken at an equivalent point in time to timeline point G in figures 2 and 3. Inset: photoelectron intensity versus time at 115 °C with molecular beam shutter periodically opened and shut (shutter status is indicated). (b) Arrhenius plot of nucleation density. Inset: PEEM images (10 μm) of the growth at various temperatures. The trend is fewer nucleation sites form at higher temperatures.

given by the deposition rate, with the actual rate at which the needle length grows compared to the width determined by the sticking/binding anisotropy.

3.4. Anisotropic molecular diffusion

In order to investigate the dynamics of the meta-stable second layer molecular diffusion a further test is employed whereby the molecular beam shutter is opened and closed several times using a time interval of roughly 150 s. This is carried out at a point in time after needles form on the surface and the de-wetting second layer reaches equilibrium (around timeline point G in figure 2(a)). In this way opening and closing the shutter can shift the equilibrium second layer density. The resultant changes in photoelectron intensity, indicating changes in layer density, are shown in the inset of figure 4(a). For an initial distribution symmetrically centred around $x = 0$, with an initial density ρ_0, the evolution of the density ρ by 1D diffusion is a function of position and time as given by $\rho(x,t) = (\rho_0/2)(\pi Dt)^{-1/2} \exp(-x^2/4Dt)$ where ρ_0 is the initial surface density and D is the diffusion coefficient, x is the position along a 1D ordinate and all other symbols have their usual meaning [18]. If one examines the time evolution at $x = 0$ it is clear that for a 1D random walk driven by diffusion the normalized surface density (ρ/ρ_0) decreases with inverse-square-root-time. Measured at several temperatures, the rise in intensity due to second layer depletion is plotted with respect to square-root-time in figure 4(a) (due to the inverse relationship between the normalized surface density and the normalized photoelectron intensity in the attenuation regime). The linearity of RT and 100 °C growth in the plot confirms that at these temperatures the molecular diffusion is 1D i.e. motion is confined along the surface corrugation. At temperatures in excess of 100 °C the increase is supra-linear, suggesting pseudo 2D diffusion due to thermal activation of molecular hopping between rows of the corrugation.

3.5. Nucleation energy and densities

As described previously the density of nucleation sites on the surface is determined at a point in time just before the de-wetting of the meta-stable second layer begins. This stochastic process is temperature dependent inasmuch as the rate of molecular de-binding events is faster at higher temperatures—hence resulting in lower survival rates of budding nucleation sites. It is when this low survival rate is translated into a probability of occurrence that the low nucleation density of 6P needles at high temperature is realized (see figure 4(b) inset). The actual mechanisms determining nuclei survivability are more complex, for instance at high temperature a stronger driving force and higher molecular mobility will push molecules faster on top of the 2D critical nucleus, however this enhancement will be offset by the shorter lifetime of the 2D nucleus due to the high de-binding rate at high temperatures. A simplified description of the nucleation process, which combines all factors that govern the nucleation by amalgamating all energy barriers into one, can be extracted from the nucleation densities for various temperatures when the rate of nucleation per unit area is plotted as an Arrhenius plot in figure 4(b). From the relationship $\mathrm{d}(\ln R_{\mathrm{nucleation}})/\mathrm{d}(1/T) = E_{\mathrm{barrier}}/k$, where $R_{\mathrm{nucleation}}$ is the rate of nucleation, T is temperature in degrees kelvin, E_{barrier} is the barrier energy and k is Boltzmann's constant, it is evident that from the measured slope there is a significant energy barrier of 675 $\pm$ 150 meV for the process of nucleation (for PTCDA on Ag(111) it is 740 $\pm$ 200 meV [12]). In the framework of the preceding discussion, the effective nucleation energy represents the energy barrier to be overcome in order to initiate a spontaneous change in arrangement type from near commensurate 2D liquid to a bulk crystal. Furthermore, the fact that the nucleation density is observed to be temperature dependent indicates that the second layer nucleation is not triggered by the arrival of molecules to a third layer from the

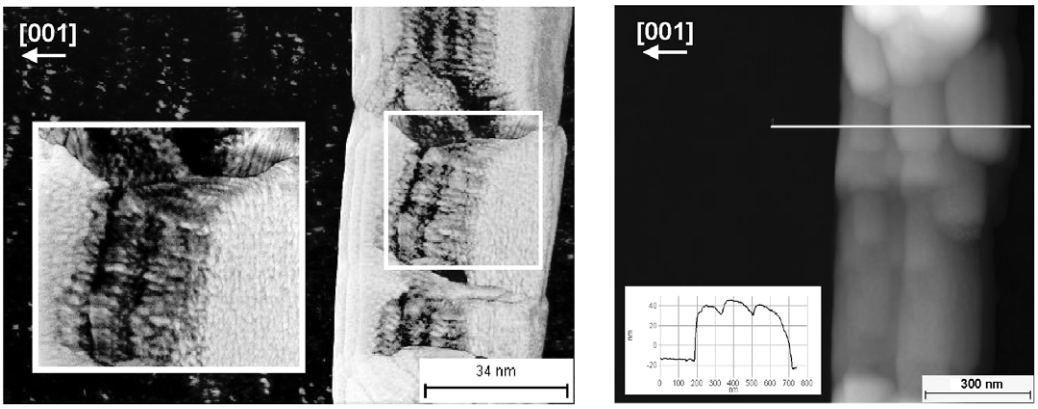

(a) (b)

Figure 5. AFM of 6 ML of 6P deposited at 140 °C on Cu(110)2 × 1–O. (a) The AFM frequency shift image, acquired in AM regulation mode in UHV, is detailed enough to show inter-grain boundaries within a needle as well as molecular steps on the needle surface (enlarged in the inset). (b) Height image of a larger 6P needle. Line profile, included as an inset, indicates the needle is ∼50 nm tall and 500 nm wide (from PEEM, length is <10 μm). Note that as the needle width increases, bunches of smaller needles (such as in (a)) give the appearance of wider needles.

evaporator. If this were the case a similar nucleation density would be observed for all temperatures.

3.6. AFM of para-sexiphenyl needles

The AFM images of needles in figure 5 are representative of needles seen in figure 1(b). As can be seen in figures 1(b) and 5, highly ordered uni-axially oriented needles of 6P are distributed on the surface. It is clear from NEXAFS [5], STM [16] and ARUPS [20] that the long axis of the needles is perpendicular to the [001] direction of the O rows. The reason for the perpendicularity of the needles to the O rows is the co-facial stacking of molecules as they join the needle. Molecules diffusing along the O rows (with their long axis parallel to the O rows) collide and stick to the needle, slot into place and are kept there by the anisotropic molecule–molecule binding. By simple deduction, if molecules diffuse on the surface and bind to the needle's end, the needle grows in length. On the other hand, if they arrive elsewhere: (a) the molecules may hop on top, increasing the needle height, or (b) bind to another molecule at the needle side and start to increase the needle width. From x-ray diffraction studies, the surface of the typical herringbone 6P crystal, which is in plane with the substrate, corresponds to the $(20\bar{3})$ surface. In this arrangement the long axis of the molecules align with the O rows as suggested by the de-wetting shape, the needle structure and the anisotropy of the molecular diffusion. Furthermore, evidence from AFM corroborates the lying down orientation of the molecules (no 2.7 nm step heights are observed which would indicate a standing orientation). AFM images in figures 5(a) and (b) clearly show that the needles are not single crystals but are rather comprised of several $(20\bar{3})$ crystalline grains with distinct inter-grain boundaries. The small needle in figure 5(a) is an example of one of the smaller crystallites that are visible in figure 5(b) which make up the needle. From the AFM images, it appears that larger needles could be described as being made up of bunches of smaller needles. Therefore it is evident that the dimensions of these grains enlarge much slower than the corresponding needle structure dimensions.

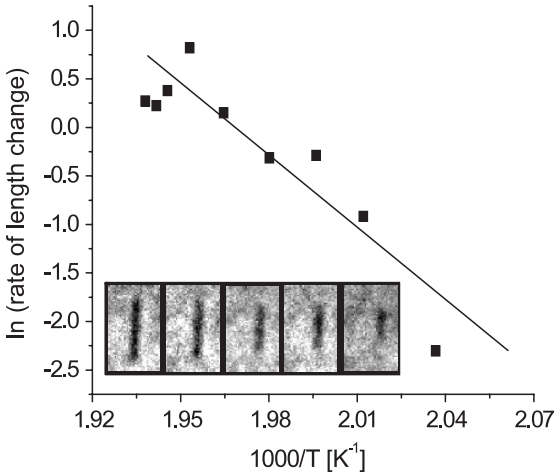

Figure 6. Arrhenius plot of 6P needle length contraction during thermal desorption to determine molecular binding energy. Inset: snap-shot PEEM images of 6P desorption demonstrating the length contraction of the needle.

3.7. Molecular binding energy measurement

In addition to growth measurements with PEEM it is also possible to monitor the disassembly of nanostructures. In this way it is possible to extract the intermolecular binding energy by heating the sample along a known temperature–time curve to above the desorption temperature and measuring the instantaneous rate of needle contraction at various temperatures. In effect the measurement probes the de-binding rate described by $\nu_0 \exp(-E_B/kT)$. As shown in figure 6, the binding energy of 6P molecules is readily accessible from the slope of the Arrhenius plot of the rate of change of the needle length during thermal desorption. The reasonable assumption required to extract the binding energy is that the process of molecular desorption from the needle is not a function of the needle length (i.e. the cross-section of the needle must be uniform through out its length) and that the exponential pre-factor ν_0 is constant. In this framework the binding energy

per 6P molecule is measured to be 2.1 ± 0.1 eV which is greater than values for 4P measured [29] by thermal desorption spectroscopy (TDS).

4. Conclusions

As has been shown with 6P, PEEM is a versatile instrument that is a valuable tool to investigate the early stage growth of molecular nanostructures during deposition. The ability to acquire, in real time, detailed photoemission intensity versus time curves allows exact amounts of material to be deposited. Likewise, the high surface sensitivity of PEEM also enables 6P molecular film relaxations at the monolayer/bilayer level to be accurately followed. These observations of dynamic dewetting phenomena described here are pivotal to understanding the formation of needles of 6P and has enabled a self-consistent two step nucleation process of forming a 3D nano-needle to be elucidated from the data. It also directly confirms the diffusion anisotropy observed separately when opening and closing the molecular beam shutter. Varying the substrate temperature in PEEM during growth allows the energetic barriers involved in growth, such as the nucleation energy, to be determined. Furthermore, by ramping the temperature to above the desorption temperature, PEEM also allows the molecule to molecule binding energy to be measured easily.

Acknowledgment

Supported by the Austrian Science Foundation (FWF).

References

[1] Choi J-H, Kim K-H, Choi S-J and Lee H H 2006 *Nanotechnology* **17** 2246
[2] Jo J, Heremans J J, Bradbury F, Chen H and Soghomonian V 2004 *Nanotechnology* **15** 1023
[3] Schwoerer M and Wolf H C 2005 *Organische Molekulare Festkörper* (Weinheim: Wiley–VCH)
[4] Al-Shamery K, Rubahn H-G and Sitter H 2008 *Organic Nanostructures for Next Generation Devices* (Berlin: Springer)
[5] Koller G, Berkebile S, Ivanco J, Netzer F P and Ramsey M G 2007 *Surf. Sci.* **601** 5683
[6] Rosei F, Schunack M, Naitoh Y, Jiang P, Gourdon A, Laegsgaard E, Stensgaard I, Joachim C and Besenbacher F 2003 *Prog. Surf. Sci.* **71** 95
[7] Blau W J and Fleming A J 2004 *Science* **304** 1457
[8] Whitesides G M and Grzybowski B 2002 *Science* **295** 2418
[9] Buckanie N M and Meyer zu Heringdorf F-J 2007 *Surf. Sci.* **601** 1701
[10] Chuang T J, Zhai R S, Chan Y L, Hsu C K, Hsub Y J, Wie D H and Klauser R 2005 *J. Electron Spectrosc. Relat. Phenom.* **144** 421
[11] Meyer zu Heringdorf F-J, Reuter M C and Tromp R M 2001 *Nature* **412** 517
[12] Marchetto H, Groh U, Schmidt T, Fink R, Freund H-J and Umbach E 2006 *Chem. Phys.* **325** 178
[13] Mundschau M, Kordesch M E, Rausenberger B, Engel W, Bradshaw A M and Zeitler E 1990 *Surf. Sci.* **227** 246
[14] Ivanco J, Haber T, Krenn J R, Netzer F P, Resel R and Ramsey M G 2007 *Surf. Sci.* **601** 178
[15] Balzer F and Rubahn H-G 2002 *Surf. Sci.* **507** 588
[16] Oehzelt M, Grill L, Berkebile S, Koller G, Netzer F P and Ramsey M G 2007 *ChemPhysChem* **8** 1707
[17] Zhang Z and Lagally M G 1997 *Science* **276** 377
[18] Jackson K A 2004 *Kinetic Processes* (Weinheim: Wiley–VCH) p 188
[19] Hu Y, Maschek K, Sun L D, Hohage M and Zeppenfeld P 2005 *Surf. Sci.* **600** 762
[20] Koller G, Berkebile S, Oehzelt M, Puschnig P, Ambrosch-Draxl C, Netzer F P and Ramsey M G 2007 *Science* **317** 31
[21] Hlawacek G, Puschnig P, Frank P, Winkler A, Ambrosch-Draxl C and Teichert C 2008 *Science* **321** 5885
[22] Park J H and Aluru N R 2007 *Chem. Phys. Lett.* **447** 310
[23] Ivanco J, Winter B, Netzer F P and Ramsey M G 2003 *Adv. Mater.* **15** 1812
[24] Berkebile S, Koller G, Hlawacek G, Teichert C, Netzer F P and Ramsey M G 2006 *Surf. Sci.* **600** 31
[25] Fleming A J, Surnev S and Netzer F P 2007 *J. Appl. Phys.* **102** 084902
[26] Ramsey M G, Schatzmayr M, Leising G and Netzer F P 1994 *Mol. Cryst. Liq. Cryst.* **256** 679
[27] Rottermund H H, Nettesheim S, von Oertzen A and Ertl G 1992 *Surf. Sci.* **275** 645
[28] Rotermund H H 1993 *Surf. Sci.* **283** 87
[29] Müllegger S and Winkler A 2005 *Surf. Sci.* **574** 322